



On-line melt pool temperature control in L-PBF additive manufacturing

Hossein Rezaeifar¹ · M. A. Elbestawi¹

Received: 25 September 2020 / Accepted: 1 December 2020 / Published online: 8 January 2021
© The Author(s), under exclusive licence to Springer-Verlag London Ltd. part of Springer Nature 2021

Abstract

Laser powder bed fusion is a promising additive manufacturing technology which has enabled the fabrication of complex-shape, custom-designed, and cost-effective parts with no need for expensive tools and dies. Despite the numerous advantages of this technology, inconsistency in the microstructure and, consequently, the mechanical properties of the fabricated components in the building direction makes it quite challenging to obtain uniform parts in the as-built state. This issue originates from the layer-by-layer melt pool temperature variation caused by the layer-wise nature of this process when a fixed set of process parameters is applied. Accordingly, a layer-wise melt pool temperature control system is beneficial in manipulating the process parameters and therefore adjusting the melt pool temperature. In this study, three different controllers, namely, simple proportional (P), adaptive P, and sliding mode, were designed to control the melt pool temperature in the building direction for Inconel 625 superalloy. An analytical-experimental model was introduced to evaluate the performance of controllers through simulation. A monitoring system having a two-color pyrometer was used to online monitor the temperature for use by the controllers as a feedback signal. The microstructure and microhardness of the final products were evaluated prior to and after employing the melt pool temperature controllers. Compared to the scenario with constant process parameters, the implementation of these controllers led to improved microhardness and microstructure uniformity, resulting from the reduced variation in the primary dendrite arm spacing. The lessons learned from this study can assist in the fabrication of functionally graded materials with engineered microstructures.

Keywords Laser powder bed fusion · Control · Melt pool temperature · Microstructure · Microhardness

Abbreviations

AM	Additive manufacturing
CAD	Computer-aided design
CMOS	Complementary metal oxide semiconductor
FGM	Functionally graded material
LI	Length of interval
L-PBF	Laser powder bed fusion
PID	Proportional-integral-derivative
PI	Proportional-integral
SEM	Scanning electron microscope
SMC	Sliding mode control

1 Introduction

Laser powder bed fusion (L-PBF) is a promising additive manufacturing (AM) technique, which has drawn a great deal of attention in recent years for fabricating complex shapes with intricate features in a layer-by-layer manner (Fig. 1) directly from a computer-aided design (CAD) model without the necessity of designing complicated build tools [1–5]. The emergence of L-PBF as a novel processing method has opened a new window to fabricate parts with unique microstructural and mechanical properties different from those produced by conventional manufacturing methods. In general, several experiments or time-consuming simulations are needed to determine the optimal process parameters alleviating the formation of defects [6]. Nevertheless, since the average temperature of the build increases gradually during the L-PBF process due to the heat accumulation phenomenon [7], a fixed set of process parameters (i.e., laser power, scanning speed, hatch spacing, and powder layer thickness) may lead to components

✉ Hossein Rezaeifar
rezaeifh@mcmaster.ca

M. A. Elbestawi
elbestaw@mcmaster.ca

¹ Department of Mechanical Engineering, McMaster University, 1280 Main Street West, Hamilton, ON L8S 4L7, Canada

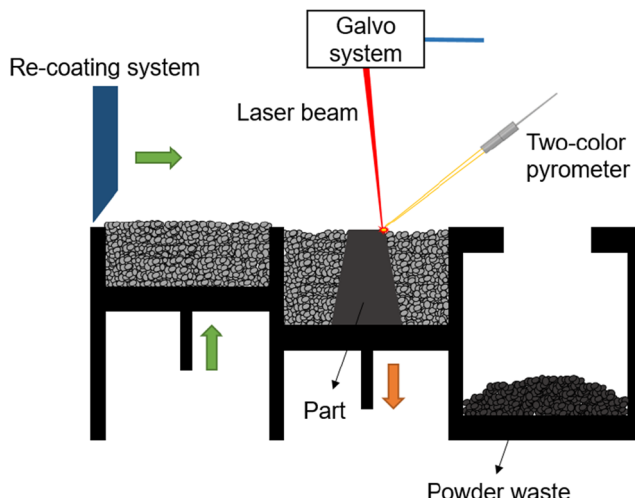


Fig. 1 Schematic illustration of a laser powder bed fusion (L-PBF) system

with non-uniform microstructure and consequently varying mechanical properties.

To address the abovementioned issue in a reasonable time, a dynamically adjustable system is essential to manipulate the process parameters to end up with a nearly constant temperature along the build. In other words, microstructure characteristics depend on the solidification process, which is directly related to the thermal dynamics of the melt pool. Therefore, it is necessary to control the thermal dynamics of the molten material to achieve desired attributes (e.g., uniform microstructure and functionally graded materials) in a cost-effective approach. Moreover, because the mechanical properties of the final parts are governed by the microstructural features, melt pool temperature control not only reduces the microstructural discrepancy but also results in consistent mechanical properties (e.g., microhardness) throughout the part [8, 9].

A few attempts have been made recently to control the L-PBF process. A study in NIST (National Institute of Standards and Technology) discussed the control requirements and its essential equipment, such as monitoring systems, laser systems, and computational resources [10]. They also explained the concept of a control system suitable for the L-PBF process. In another study, a coaxial monitoring system consisting of a photodiode and a complementary metal oxide semiconductor (CMOS) camera was employed to control the melt pool area [11]. By applying a first-order transient behavior for the transfer function between the melt pool area and laser power, the fabrication of overhang structures was improved when a proportional-integral-derivative (PID) controller was utilized.

According to a latter work conducted by the same authors [12], a photodiode was used to transmit melt pool area information, and a proportional-integral (PI) controller was utilized to enhance the dimensional accuracy in two different cases, namely, slow scanning speed and downfacing surface condition. However, both studies shared the same drawback of using a PID controller with fixed parameters, which lacks to guarantee a robust controlling for different conditions in the nonlinear AM processes. Besides, by considering the proportional relation between the photodiodes signals and the melt pool area [11], the output voltage from the photodiodes is quite small in comparison to the real values of the melt pool area. Therefore, a small error in the results leads to a considerable error in the melt pool area measurements, making the melt pool unstable. The EU-founded project MEGAFiT established a study on controlling the AM process by means of a thermal camera, a color sensor, and a topography sensor. After introducing the concept of their control design [13], three proportional (P) controllers with different gains were designed to control the melt pool temperature by a pyrometer [14]. However, output values were reported in voltage, the same as [11], and the controller had a fixed gain. Besides, a comparison among a P controller, a model-based feedforward controller, and the combination of these two controllers was implemented to evaluate the improvement in the quality of the bridge structure [15]. In all studies mentioned above, the quality of the parts was examined in a macro-scale, while micro-scale features dictating the mechanical properties were ignored. Therefore, microscopic features should be scrutinized from the control point of view.

This research study, for the first time, proposes an adaptive P controller and a sliding mode controller (SMC) to control the melt pool temperature of Inconel 625 superalloy in the L-PBF process by manipulating the laser power. The conventional simple P controller was also implemented as a reference to evaluate the performance of the newly proposed control systems in terms of the rise time and robustness against disturbances. For this purpose, a model that simulates the L-PBF process is first suggested and validated by experimental measurements using a two-color pyrometer calibrated in advance. Then, the responses of the proposed controllers are simulated. Finally, the controllers are experimentally implemented in the L-PBF machine. Using the proposed controllers and setting two different reference temperatures, the influence of the controller type and the temperature on the microstructure and microhardness of the fabricated parts is investigated and compared with the uncontrolled scenario. The knowledge gained from the microstructural characterization and microhardness measurements

Table 1 Material properties of Inconel 625 used for the simulation [16]

Laser absorption η (%)	Thermal conductivity k (W/m – °C)	Thermal diffusivity κ (mm ² /s)
40	9.8	2.71

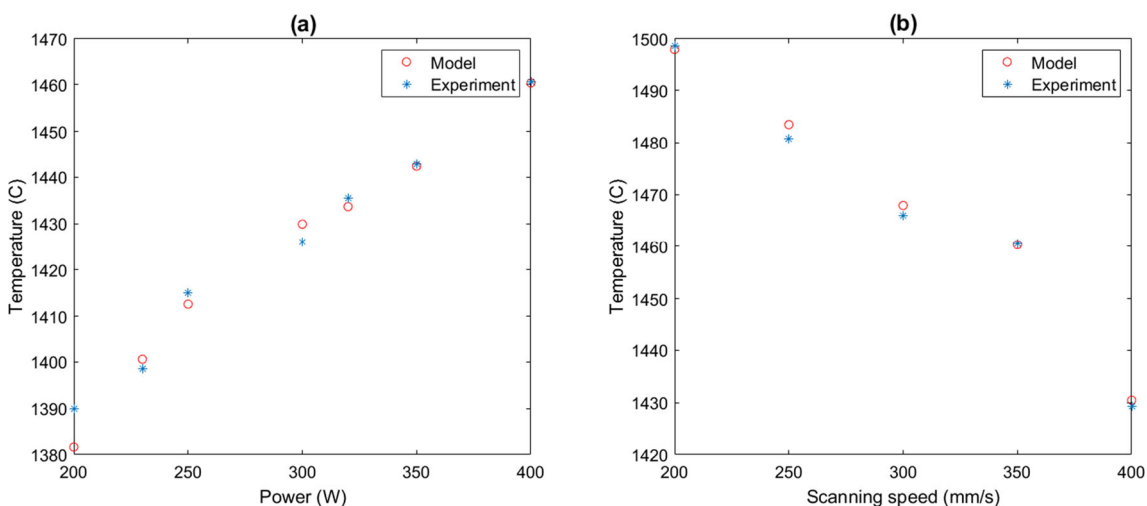


Fig. 2 **a** Variations of the melt pool temperature as a function of the laser power in the fixed scanning speed of 350 mm/s, and **b** effect of the scanning speed on the melt pool temperature under the fixed laser power of 400 W

reinforce the idea that the application of an appropriate control system can not only reduce the microstructural and microhardness variations in the building direction but also provide the opportunity to fabricate functionally graded materials (FGM).

2 Modeling and control strategies

2.1 Simulation modeling

Different modeling methods are utilized to check the controller response before running an experiment. Among those, analytical modeling and system identification approaches are used for control purposes since the numerical method is extremely time-consuming, while a fast response is required for a control system.

An analytical model has been proposed by Ning et al. [16] using a moving point heat source solution, which was originally propounded by Carslaw and Jaeger [17] to find the temperature distribution profile inside and around the melt pool. Although the radiation and convection heat transfers are

ignored in this equation, the laser absorption coefficient, latent heat of fusion, and powder packing density have been taken into consideration:

$$\theta(x, y, z, t) = \frac{P\eta}{2Rk\pi^{\frac{3}{2}}} \exp\left(\frac{Vx}{2\kappa}\right) \int_{\frac{R}{2\sqrt{\pi t}}}^{\infty} \exp\left[-\xi^2 - \left(\frac{V^2 R^2}{16\kappa^2 \xi^2}\right)\right] d\xi \quad (1)$$

where P , η , V , k , t , and κ denote the laser power, laser absorption coefficient, laser scanning velocity, thermal conductivity coefficient, current time, and thermal diffusivity, respectively. ξ is an integral variable. The terms “ θ ” and “ R ” in Eq. (1) are temperature change and distance, respectively, defined as:

$$\theta = T - T_0 \quad (2)$$

$$R^2 = x^2 + y^2 + z^2 \quad (3)$$

in which T_0 and T signify the initial temperature and the current temperature of the desired location and time, respectively. x , y , and z specify each point uniquely in the Cartesian

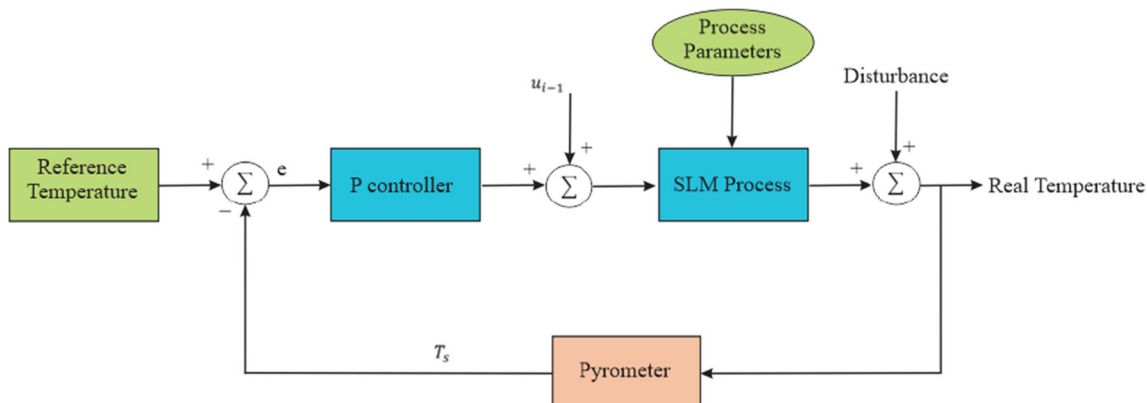


Fig. 3 Block diagram of the employed P controller

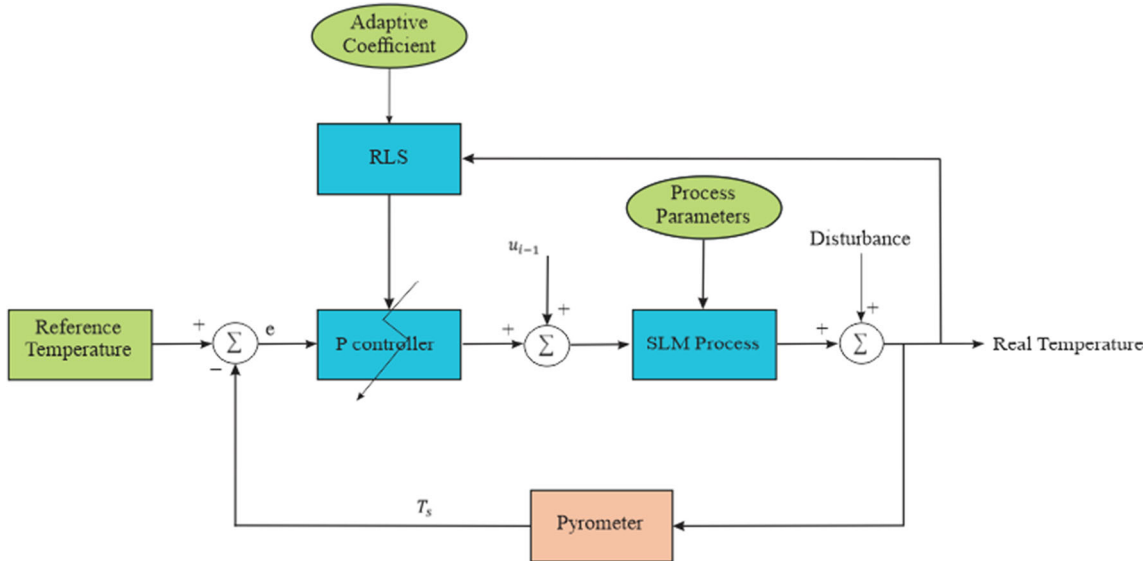


Fig. 4 The block diagram of the adaptive P controller. The coefficient of the controller is updated after printing each layer

coordinate system. Given the fact that the temperature of a certain location on each layer at a known time is required in this study, and the scanning speed is constant during the control process (V_e), t can be substituted by $\frac{x}{V_e}$. In addition, since the temperature of a single point in each layer is measured by the pyrometer, it is not essential to have the temperature distribution profile ($y=0$ and $z=z_s$). Therefore, Eq. (1) can be rewritten as presented in Eq. (4).

$$\theta\left(x, 0, z_s, \frac{x}{V_e}\right) = \frac{P\eta}{2Rk\pi^{\frac{3}{2}}} \exp\left(\frac{V_ex}{2\kappa}\right) \int_{\frac{R}{2\sqrt{\pi V_e}}}^{\infty} \exp\left[-\xi^2 - \left(\frac{V_e^2 R^2}{16\kappa^2 \xi^2}\right)\right] d\xi \quad (4)$$

In Eq. (4), z_s is the height of the measuring point. According to the model in Eq. (1), the temperature of the molten material for Inconel 625 was reported to be 4000 °C, which is unrealistic because evaporation would happen at this high temperature. In addition, the model suffers from a

singularity problem. In this study, the model is constructed based on Eq. (4), while experimental data are also used to correct the abovementioned issues. By defining a variable $B_c = f(P, V)$ to solve this, the final equation will be as follows:

$$\theta\left(x, 0, z_s, \frac{x}{V_e}\right) = \frac{P\eta B_c}{2\pi^{\frac{3}{2}}} \exp\left(\frac{V_ex}{2\kappa}\right) \int_{\frac{R}{2\sqrt{\pi V_e}}}^{\infty} \exp\left[-\xi^2 - \left(\frac{V_e^2(x^2 + z_s^2)}{16\kappa^2 \xi^2}\right)\right] d\xi \quad (5)$$

The thermophysical material properties of the Inconel 625 are listed in Table 1. The function f has been obtained by implementing several experiments, including 12 random laser powers from 150 to 400 W and 10 random scanning speeds from 200 to 600 mm/s (120 experiments) with fixed hatch spacing and layer thickness. By polynomial fifth-order approximation, the following equation can be drawn:

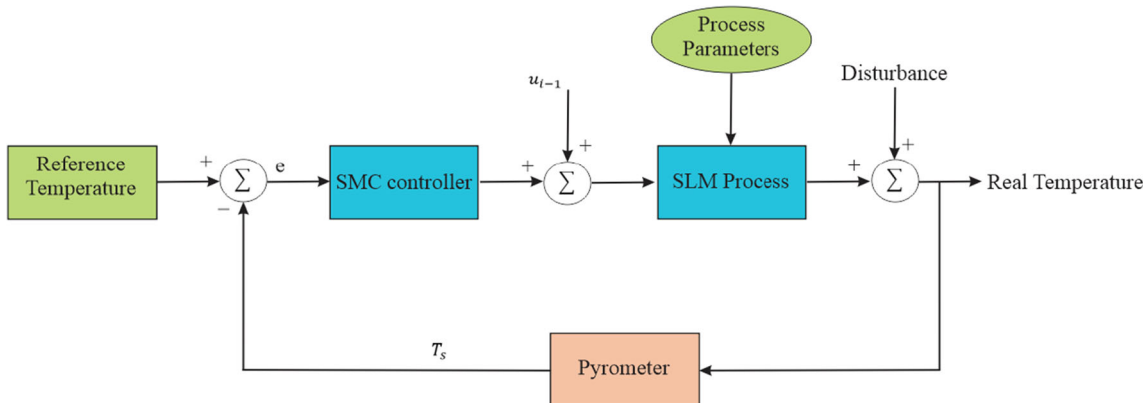


Fig. 5 Sliding mode control block diagram

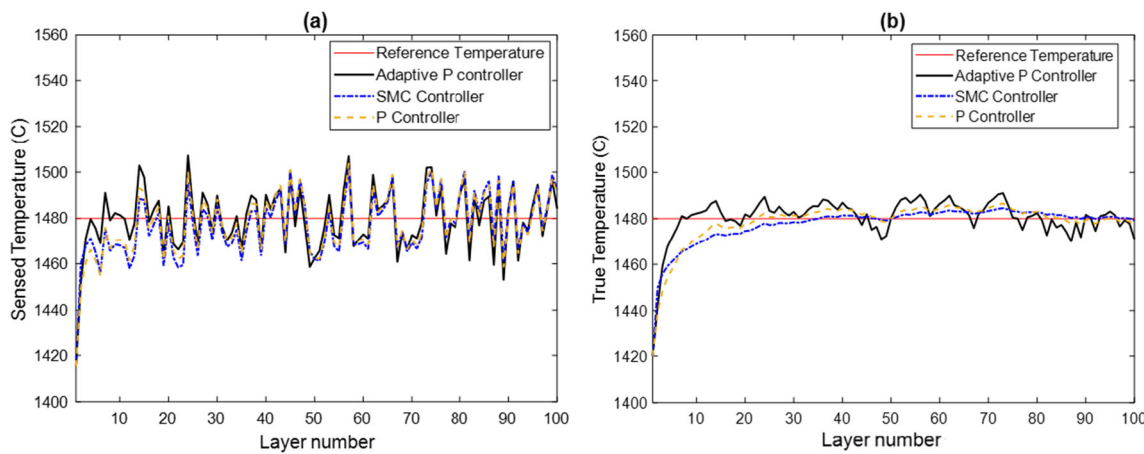


Fig. 6 **a** The temperature sensed by the virtual sensor with an identical noise and error for all controllers, and **b** the true temperature calculated by the model based on the controllers' command. The adaptive controller

$$B_c = \sum_{n=0}^5 \sum_{m=0}^5 p_{nm} P^n V^m \quad (6)$$

where p represents the coefficient of the polynomial function while n and m are integers from 0 to 5.

The modeling results are depicted in Fig. 2. For validating the results, a pyrometer has been employed to measure the melt pool temperature (Fig. 1). Based on Fig. 2, it is self-evident that the model outputs are in good agreement with the experimental results achieved by two measurement approaches for the mentioned range of laser power and scanning speed. The temperature shows an ascending trend by increasing the laser power and a descending trend by increasing the scanning speed as expected. It should be born in mind that by increasing the laser power or decreasing the scanning speed, the melt pool size is enhanced, and the level of evaporation is increased as well. Therefore, the melt pool resists against a huge change in temperature. The response

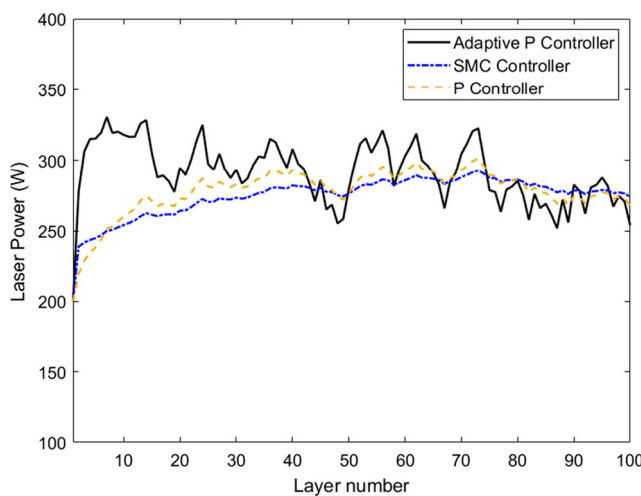


Fig. 7 The laser power in each layer for different controllers when a fixed desired temperature is set (first scenario)

responded faster while the sliding mode controller was more robust against noises and errors

of the control systems using this model is discussed in Section 2.2.4.

2.2 Controller design

The models of the AM processes have a lot of time-varying parameters and coefficients, such as laser power absorption, conductivity, and diffusivity of the material. Additionally, there is a dynamic environment inside the chamber that can alter the process and measurements. For instance, vapor and dust change the ratio of radiation energy, which is the basis of the temperature measurement. According to [18–20], PID controllers with fixed gains are sensitive to the abovementioned processes and adaptive gains, and nonlinear controllers provide better results in such conditions.

In this study, a feedback control system using signals achieved by the pyrometer was implemented. Three different

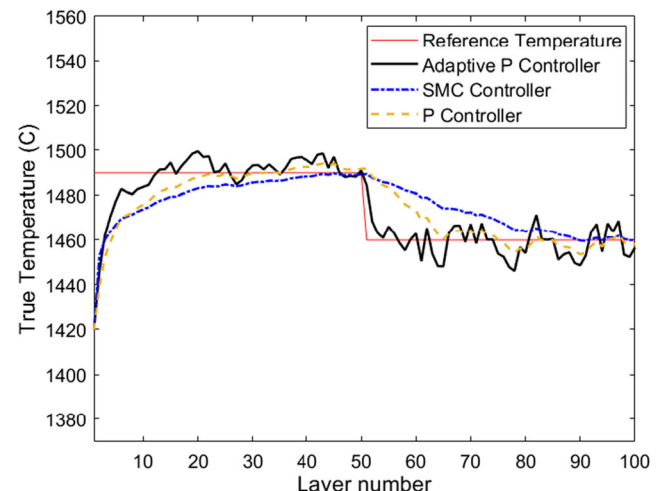


Fig. 8 The true temperature when two different reference temperatures were set (second scenario). The SMC is noticeably slow to switch between two desired temperatures

Table 2 Performance analysis of controllers in two different scenarios

	P controller	Adaptive P controller	SMC controller
J in scenario 1	5632.9	4715.5	3137.9
J in scenario 2	13,448	8138.2	16,175

types of controllers, including conventional P, adaptive P, and SMC, were investigated, and results were compared.

2.2.1 P controller

According to Fig. 3, the error in the loop can be obtained by subtracting the reference temperature from the signal captured by the pyrometer as:

$$e = T_r - T_s \quad (7)$$

where T_r is the reference temperature, and T_s is the temperature sensed by the pyrometer. The P controller with the proportional gain k_p calculates the laser power output, u_i , at the layer i as:

$$u_i = u_{(i-1)} + k_p \cdot e \quad (8)$$

Based on Eq. (8), the controller output is obtained by adding the proportional section to the previous laser power. The controller output was limited between 170 and 400 W since the laser system of the machine cannot work over 400 W, and the system identification has been applied in this range.

2.2.2 Adaptive P controller

By considering the first layer and Eq. (5) in the modeling section, the temperature of the scanned point captured by the pyrometer has a direct relation with the initial laser power $u(0)$ and the initial temperature of the powder layer $T_0(1)$, which is considered to be equal to the environment temperature.

$$\begin{aligned} T_1(x_L, y_L, 0, t_L) \\ = \frac{P\eta B_c}{2k\pi^{\frac{3}{2}}} \exp\left(\frac{V_e x_L}{2\kappa}\right) \int_{\frac{R}{2\sqrt{\pi t_L}}}^{\infty} \exp\left[-\xi^2 - \left(\frac{V_e^2 R^2}{16\kappa^2 \xi^2}\right)\right] d\xi \\ + T_0(1) \Rightarrow T_1 \rightarrow u(0), T_0(1) \end{aligned} \quad (9)$$

After the laser beam scanned the first layer, the exposed material cools down through convection, radiation, and conduction heat transfer mechanisms in a certain amount of time. All these heat transfer mechanisms have a direct relationship with the measured temperature of the first layer (T_1), so that

$$e(i) = T_r(i) - T(i) = T_r(i) - [a(i)u(i-1) + b(i)u(i-1)] = T_r(i) - [b(i)[u(i-2) + k_p[T_r(i-1) - [a(i-1)T(i-2) + b(i-1)u(i-2)]]] + a(i)T(i-1)] \quad (15)$$

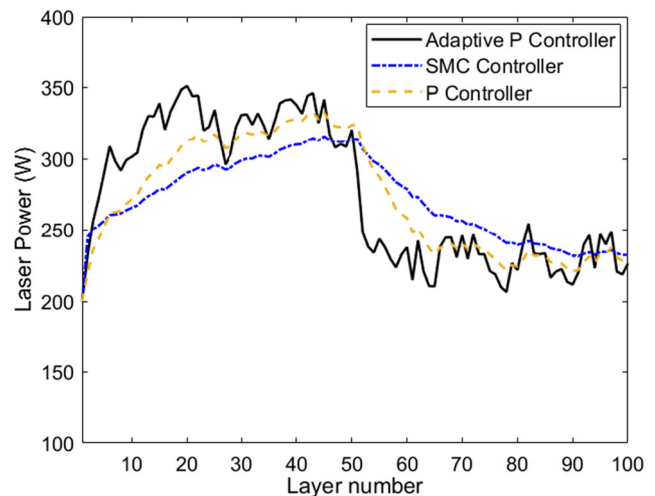


Fig. 9 The laser power when two different reference temperatures were set (second scenario)

the initial temperature for the second layer is related to the captured temperature of the first layer. Therefore, the temperature of the second layer is affected by $u(1)$ and T_1 as follows:

$$T_2(x_L, y_L, 0, t_L)$$

$$\begin{aligned} &= \frac{P\eta B_c}{2k\pi^{\frac{3}{2}}} \exp\left(\frac{V_e x_L}{2\kappa}\right) \int_{\frac{R}{2\sqrt{\pi t_L}}}^{\infty} \exp\left[-\xi^2 - \left(\frac{V_e^2 R^2}{16\kappa^2 \xi^2}\right)\right] d\xi \\ &+ T_0(2) \Rightarrow T_2 \rightarrow u(1), T_0(2) \text{ or } u(1), T_1 \end{aligned} \quad (10)$$

Hence, the discrete model of the process can be explained as:

$$T(k) = a(k)T(k-1) + b(k)u(k-1) \quad (11)$$

Equation (11) is used as a process model in designing the adaptive controller. The aim of using this controller is to make the temperature error equal to zero. Using Eqs. (7), (8), and (11), the error can be derived as Eq. (15).

$$T(i-1) = a(i-1)T(i-2) + b(i-1)u(i-2) \quad (12)$$

$$\begin{aligned} e(i-1) &= T_r(i-1) - T(i-1) \\ &= T_r(i-1) - [a(i-1)T(i-2) + b(i-1)u(i-2)] \end{aligned} \quad (13)$$

$$\begin{aligned} u(i-1) &= u(i-2) \\ &+ k_p[T_r(i-1) - [a(i-1)T(i-2) + b(i-1)u(i-2)]] \\ &+ k_p[T_r(i-1) - [a(i-1)T(i-2) + b(i-1)u(i-2)]] \end{aligned} \quad (14)$$

Table 3 The nominal chemical composition of the Inconel 625 used in this study

Element	Al	C	Co	Cr	Cu	Fe	Mo	Mn	Nb+Ta	Ni	P	S	Si	Ti
Min (wt%)	-	-	-	20.0	-	-	8.0	-	3.15	Bal	-	-	-	-
Max (wt%)	0.4	0.1	1.0	23.0	0.5	5.0	10.0	0.5	4.15	Bal	0.015	0.015	0.5	0.4
Result	0.11	0.02	0.02	22.0	< 0.1	0.3	9.0	< 0.01	3.80	Bal	< 0.001	0.001	0.07	0.11

In order to have $e(i)=0$, the proportional gain will be:

$$k_p = \frac{T_r(i-1)-a(i)T(i-1)-b(i)u(i-2)}{b(i)[T_r(i-1)-a(i-1)T(i-2)-b(i-1)u(i-2)]} \quad (16)$$

Using recursive least square (RLS) estimation, the terms a and b can be determined [21]. The model presented in Eq. (11) can be rewritten as:

$$y(k) = \emptyset^T(k)\hat{\theta}(k) \quad (17)$$

$$\emptyset(k) = [-T(k-1) \ u(k-1)]^T \quad (18)$$

$$\hat{\theta}(i) = [\hat{a}(i), \hat{b}(i)]^T \quad (19)$$

where $\emptyset(k)$ is data vector, and $\hat{\theta}$ is the parameter vector. The cost function is:

$$J(\hat{\theta}, k) = \frac{1}{2} \sum_{i=1}^k \lambda^{k-i} [y(i) - \emptyset^T(i)\hat{\theta}(i)]^2 \quad (20)$$

The recursive solution for minimizing the cost function is:

$$\hat{\theta}(k) = \hat{\theta}(k-1) + L(k)(y(k) - \emptyset^T(k)\hat{\theta}(k-1)) \quad (21)$$

**Fig. 10** A general view of the setup used to calibrate the pyrometer

$$L(k) = \frac{P(k-1)\emptyset(k)}{\lambda I + \emptyset^T(k)P(k-1)\emptyset(k)} \quad (22)$$

$$P(k) = (I - L(k)\emptyset^T(k)) \frac{P(k-1)}{\lambda} \quad (23)$$

in which λ is the exponential forgetting factor, L represents the gain vector, and P is the error covariance matrix. $\lambda = 0.99$, since the process has disturbance and slow changes. Figure 4 shows the block diagram of the adaptive P controller.

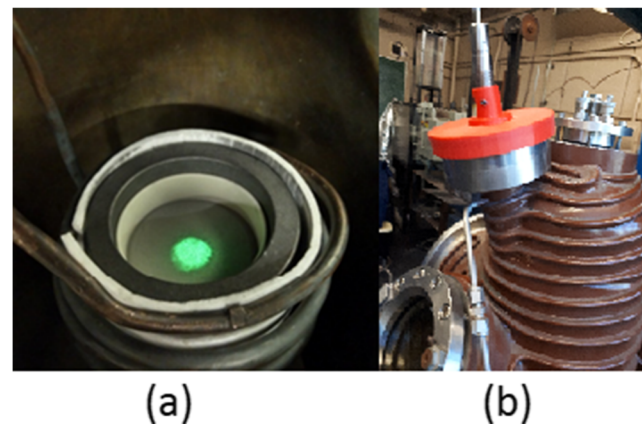
2.2.3 Sliding mode controller

For the SMC, the discrete controller presented in [22] is used to control the temperature, the only difference being that not only the coefficient corresponding to the states but also other parameters are considered to be time-variant in the model. The sliding surface is:

$$S(k) = C(T(k) - T_r(k)) \quad (24)$$

where $C = 1$ based on the model presented in Eq. (11). The sliding dynamics is defined as $S(k) = 0$ which is asymptotically stable. In this case, the controller output will be:

$$u(k) = u(k-1) + [Cb(k)]^{-1}[(\gamma-1)S(k) - C[a(k)T(k) - a(k-1)T(k-1)]] \quad (25)$$

**Fig. 11** **a** Overview of the crucible with the pyrometer spotted area, and **b** pyrometer configuration on the vacuum induction furnace

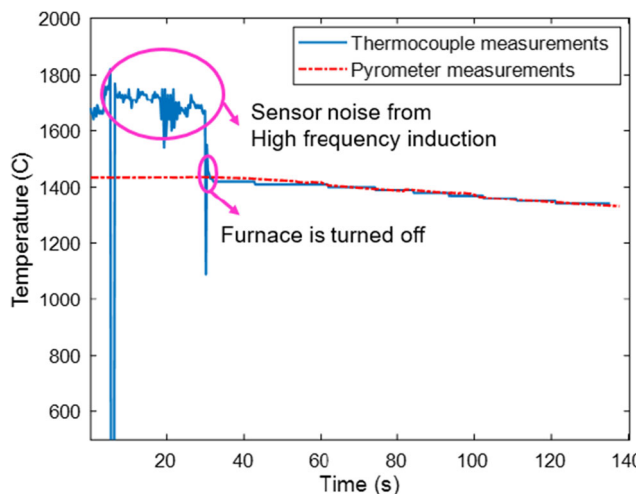


Fig. 12 Diagrams showing temperature versus time for the measurements performed by the thermocouple and pyrometer. The results were in agreement when the slope coefficient was 0.96

in which $u(k)$ is the laser power calculated for the layer $(k+1)$, and γ is an arbitrary number such that $S(k+1) = \gamma S(k)$ is asymptotically stable ($|\gamma| < 1$). The schematic of the SMC controller is presented in Fig. 5.

2.2.4 Simulation results

For comparing the performance of controllers, the sum of the squared error is used, as defined in Eq. (26):

$$J = \sum_{i=1}^N (T_r(i) - T(i))^2 \quad (26)$$

An identical noise that simulates the noise and errors of the sensor was applied to all systems with different controllers. Figure 6(a) represents the results of the three control systems. As it is evident, the applied noise is significant in the process. The true temperature, which is calculated by the model in Eq. (5), is shown in Fig. 6(b). All the controllers were successful in keeping the temperature around the desired value. The following points can be extracted from Fig. 6:

1. The response time of the adaptive P controller is shorter than the other ones.

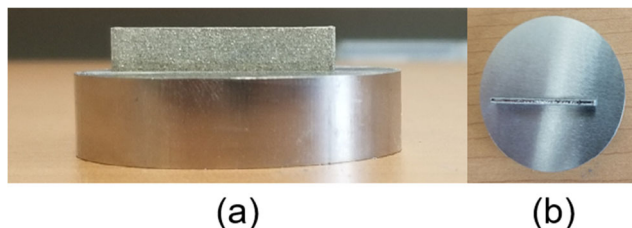
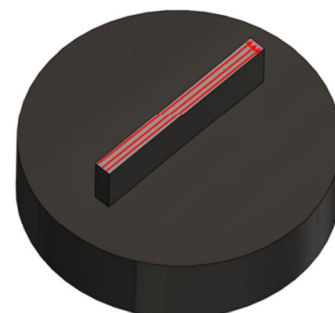
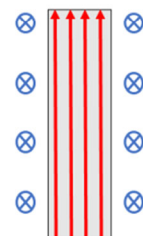


Fig. 13 The (a) side view and (b) top view of the thin wall printed on the disk

Shielding gas flow direction



(a)



(b)

Fig. 14 **a** A 3D view of the scanning pattern and the shielding gas flow direction, and **b** 2D view of scanning pattern with shielding gas flow direction flowing from the top of the chamber toward the build plate (blue cross)

2. The sum of the squared error in the SMC controller is the minimum among the others (Table 2).
3. Compared to the others, the SMC controller is more robust against the applied noise.

Figure 7 shows the input laser power for each layer using different controllers. It emphasizes that the adaptive P controller increases the laser power drastically at the start of the process, making the melt pool temperature closer to the desired temperature faster than the two other controllers.

To investigate the controllers more precisely, another scenario with two different temperatures was designed. Figure 8 shows the results of three controllers in the second scenario. The main findings from Figure 8 are as follows:

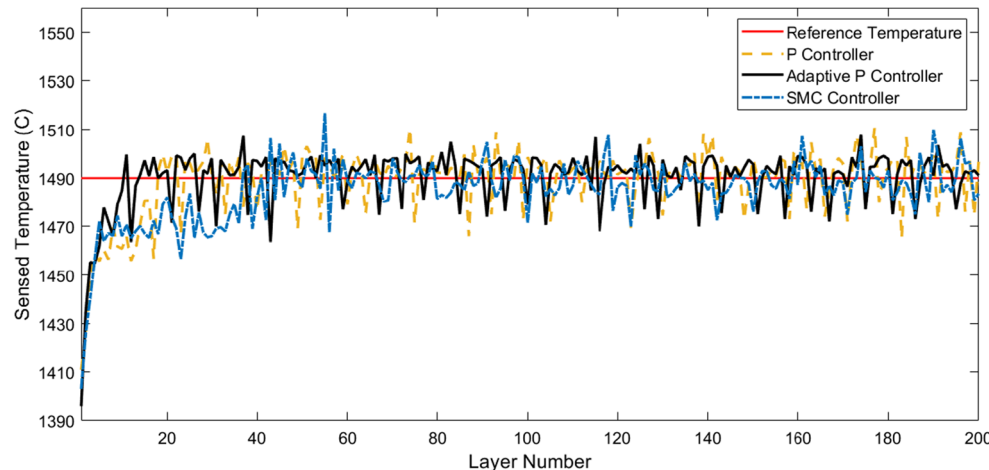
1. The SMC is too slow to reach the second desired temperature.
2. The adaptive P controller performed better than other controllers in this case (Table 2).
3. The response time of the adaptive P controller is considerably shorter than the others (Figs. 8 and 9).

In summary, the adaptive P controller performed better than two others in the simulation study, although, in some layers, it had a higher error. In Section 4, these controllers are compared from the part microstructure point of view.

3 Experimental setup

The L-PBF machine deployed in this study was OmniSint-160 having a 400-W Yb-fiber laser with a spot size of 100 μm . The

Fig. 15 The temperature sensed by the pyrometer for all controllers (1st set). The adaptive P controller responded faster compared to the other controllers



printing process was performed under the protection of a high-purity argon gas atmosphere. Laser power, which is a critical process parameter in the AM process, can be changed between layers in this machine, enabling the control of the process.

The material used in the study was Inconel 625 in the form of powder with the chemical composition provided in Table 3.

The monitoring system consists of a two-color pyrometer, capable of measuring the highest temperature in its spot area. The detectable temperature range of this pyrometer lies between 1000 and 3200 °C, with a sample rate of 1 kHz. The spot size of the pyrometer is 800 μm. Before using a contactless temperature measurement system such as a pyrometer, it is essential to know some properties of the material under investigation, specifically, the emissivity of the material. In the case of a two-color pyrometer, it is necessary to adjust the emissivity slope of the device (the ratio of emissivity at two wavelengths). The most effective way to determine and adjust the slope is to take the temperature of the material using a probe sensor such as a thermocouple or other suitable devices. Once the sensor determines the actual temperature, the slope setting should be adjusted until the pyrometer reads

the same temperature as the actual one. To perform this procedure for Inconel 625, a vacuum induction furnace with an argon gas atmosphere was used to heat the sample. It is a very suitable environment, resembling that of the L-PBF machine in which the sensor is used. The setup is shown in Fig. 10. A B-type thermocouple was used as a probe sensor to measure the actual temperature. The Inconel 625 powder was melted in a crucible and was spotted with the pyrometer (Fig. 11).

The final result of the calibration is shown in Fig. 12. The noise at the beginning of the thermocouple curve is due to the Eddy currents induced by the induction coil on the thin thermocouple leads.

As soon as the current is reduced to zero, the signal becomes noise-free. In Fig. 12, there is a strong agreement between the pyrometer and thermocouple temperature readings.

The investigation procedure and control process were carried out on a thin wall with dimensions of 1.5 × 35 × 8 mm, printed on a small disk (Fig. 13). The scanning speed, hatch spacing, and layer thickness were 200 mm/s, 80 μm, and 40 μm, respectively, throughout the experiment. Also, the initial laser power was 200 W, which was manipulated by

Fig. 16 The laser power versus the layer number for different controllers (1st set)

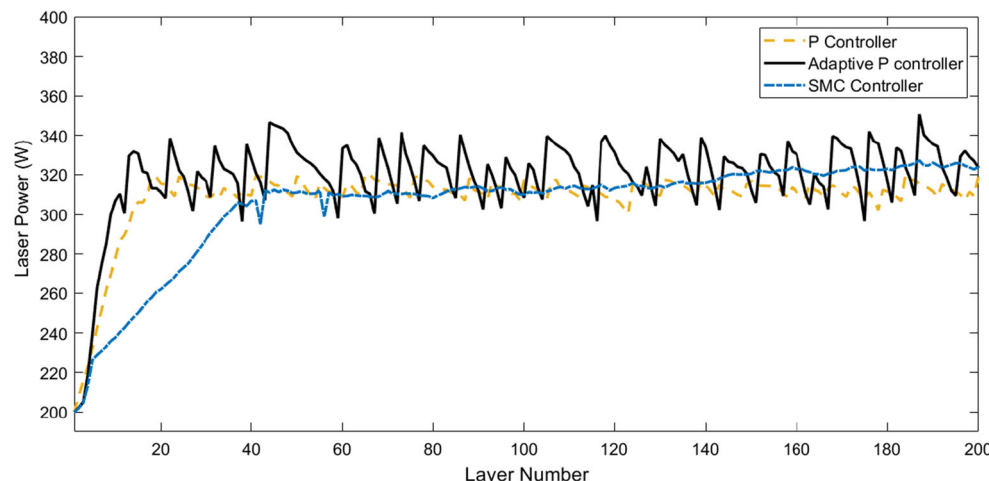


Table 4 The evaluation of the controller performance in the 1st set of experiments

Controller	Mean temperature (Layer 1 to 200)	Standard deviation (Layer 1 to 200)	Mean temperature (Layer 40 to 200)	Standard deviation (Layer 40 to 200)
Simple P	1489.2	13.95	1492.09	9.29
Adaptive P	1490.3	12.42	1491.95	8.2
SMC	1485.08	13.02	1489.35	7.64

the controllers in the subsequent layers. Based on the scanning speed, spot size, and sampling rate of the pyrometer, the melt pool fell into the spot area of the pyrometer. The scanning pattern and the shielding gas flow direction are shown in Fig. 14. The argon gas was being fed from the top of the process chamber toward the build plate during the L-PBF process. A sequential scanning pattern with no rotation between the subsequent layers was utilized for all of the samples. It should be mentioned that control systems were performed using LabVIEW on the Omnisit-160 L-PBF machine.

It is of note that no geometrical defects (in macro-scale) were observed even in the part manufactured by the fixed laser power since the process parameters were selected to be close to those leading to the defect-free Inconel 625 parts.

The fabricated thin walls were sectioned along the building direction, and microstructural investigations were performed on the cross-sections. The standard metallographic technique was used to prepare samples. For microstructural examinations, mixed acid etchant with the following composition was used: HCl-75 ml and HNO₃-25 ml. Detailed imaging of the microstructure was conducted by a TESCAN VEGA scanning electron microscopy (SEM) working at 20 kV accelerating voltage. The Image-J Software was utilized to calculate the intercellular spacing known as the primary dendrite arm spacing (PDAS) based on the SEM images.

The microhardness test was conducted on different locations of the cross-section with an applied load and dwell time of 200 g and 10 s, respectively.

Table 5 The evaluation of the controller performance in the 2nd set of experiments

Controller	Mean temperature (Layer 1 to 200)	Standard deviation (Layer 1 to 200)	Mean temperature (Layer 40 to 200)	Standard deviation (Layer 40 to 200)
Simple P	1449.6	11.78	1450.92	10.38
Adaptive P	1450.26	12.83	1450.9	12.04
SMC	1449.43	11.26	1450.35	9.67

4 Results and discussions

4.1 Control performance

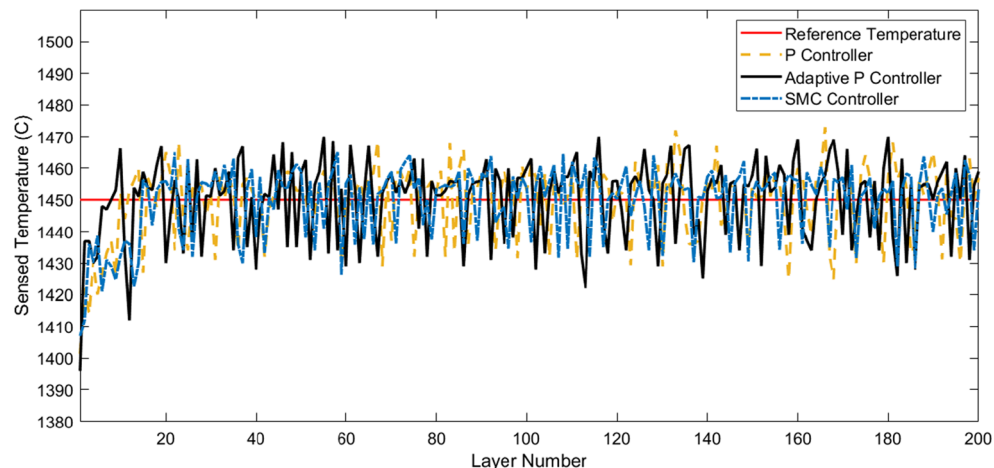
The performance of the controllers was investigated by two sets of experiments with different reference temperatures. For this purpose, a thin wall with 200 layers was fabricated using an initial laser power of 200 W and reference temperatures of 1490 °C (1st set) and 1450 °C (2nd set). The reference temperatures were chosen based on the range of the melt pool temperatures in the nearly defect-free zone acquired by pre-experiment. A total of 140 °C (first set of the experiment) and 100 °C (second set of the experiment) degree of overheating with respect to the liquidus temperature did not result in any macro-scale defects such as warpage and delamination (Fig. 13).

As mentioned, the temperature was measured in each layer at a fixed location. Figure 15 represents the temperature measurements using three controllers for the 1st set. Besides, the laser power in each layer, which was decided by the controllers for the first set, is shown in Fig. 16. The adaptive P controller, SMC, and simple P controller reached the desired temperature after 10, 18, and 37 layers, respectively. Therefore, the rise time of the adaptive P controller is significantly shorter than that of the other controllers. This feature can be useful when the purpose of control is jumping to a specific temperature at a specific height of the part. For example, when FGM is the aim of the fabrication, the adaptive P controller reacts faster to any deviation from the reference temperature in comparison to the other controllers. In addition, as mentioned in Section 2.2.4, the SMC is more robust against external disturbances.

In contrast, the adaptive P controller behaves more aggressively compared to other controllers. Referring to Table 4, it is reasonable to conclude that the adaptive P controller works more efficiently when the application requires fast response, owing to the fact that the mean temperature in this scenario is closer to the reference temperature. Moreover, the standard deviation of the data captured by the pyrometer for the adaptive P controller is smaller than those of the other controllers. However, if the abovementioned terms are investigated after a specific layer number above which all controllers have reached the desired temperature (e.g., layer 40), the SMC has the lowest standard deviation. Thus, if the initial layers are of lower importance (parts with support structures), the SMC can be a competitor to the adaptive P controller for controlling the melt pool temperature of the top layers.

Figure 17 shows the temperature measurements for the 2nd set of experiments, in which the difference between the initial temperature and the desired temperature is smaller than the 1st set. In this set, the temperature with all controllers reached the desired temperature significantly sooner, and their rise times were closer compared to the 1st set. After 8, 10, and 15 layers,

Fig. 17 The temperature sensed by the pyrometer for all controllers (2nd set)



the desired temperature was achieved by the adaptive P controller, simple P controller, and the SMC, respectively. Therefore, knowledge about the initial error can be valuable in the control process. It is worth mentioning that different gains were tested in simulation for the simple P controller to reach the best gain that works for both desired temperatures. Otherwise, for each specific temperature, a particular gain should be set using several experiments [14]. Table 5 shows the mean temperature and the standard deviation of the data for the 2nd set of experiments and confirms the points discussed based on Table 4.

4.2 Microstructure results

To investigate the effect of the temperature control on the microstructure of the final products, a thin wall was also fabricated with a fixed laser power of 250 W as the reference sample. All parts were cut from the pyrometer spot location in the vertical direction. Then, they were divided into three distinct regions (bottom, middle, and top), as shown in Fig.

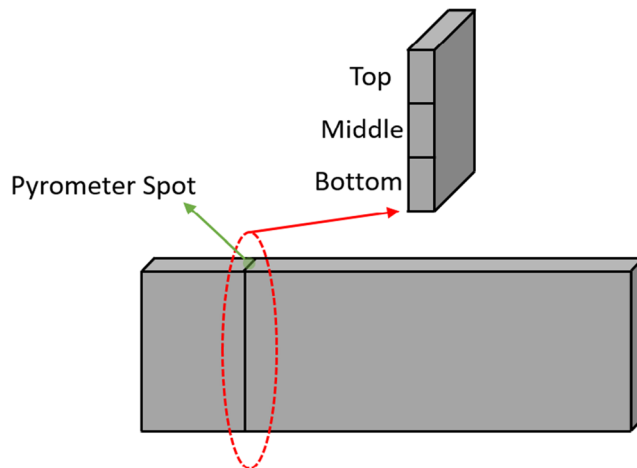


Fig. 18 The cutting location of the final parts along with the regions in which the microstructural characterization was performed

18. The microstructural features of each region were scrutinized based on SEM micrographs.

According to [23], the microstructure of the Inconel 625 part fabricated by the L-PBF process is in the cellular dendritic form. The primary dendrite arm spacing (PDAS) (Fig. 19) was used as a metric for microstructural characterization purposes. After gathering the images, the PDAS of different sections were measured. The Image-J Software was utilized to measure the PDAS of controlled and uncontrolled parts. The field of view for the measurement of the PDAS was $30 \times 30 \mu\text{m}$. The reported values for each case are the average of at least twenty distinct measurements on different images.

Figure 20 represents the measurements of the PDAS in different cases of the 1st set of experiments in different regions. It indicates that regardless of the regions, the length of interval (LI) of the PDAS became shorter when a controller was employed during the process. Figure 21 shows the

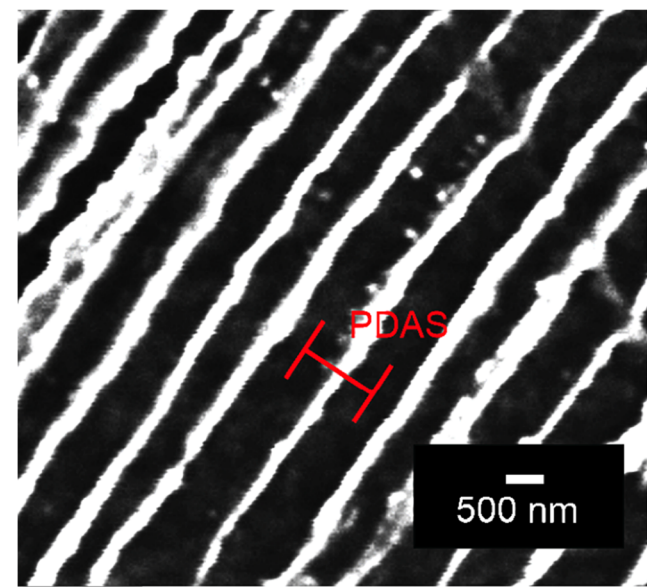


Fig. 19 SEM micrograph showing the primary dendrite arm spacing (PDAS)

Fig. 20 PDAS variations in different regions while using fixed laser power and controllers for the desired temperature of 1490 °C (1st set)

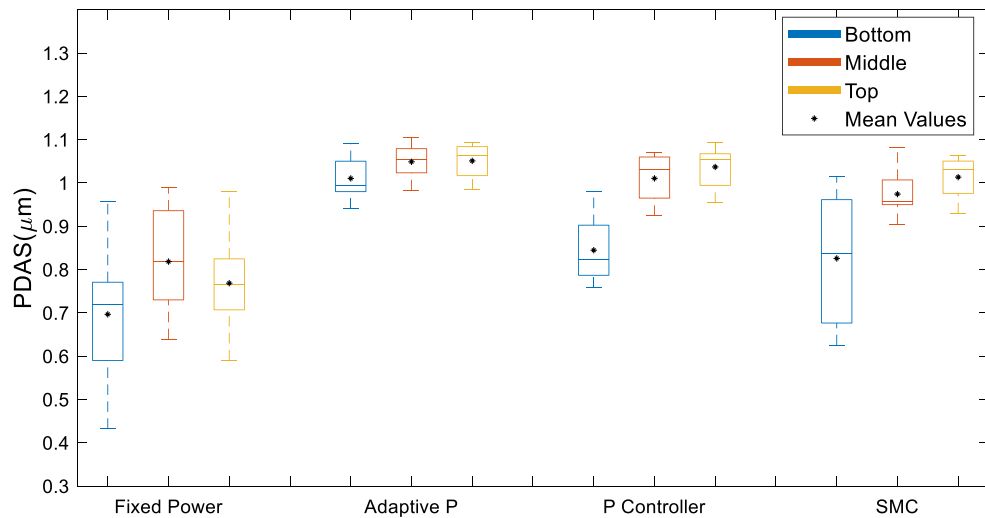


Fig. 21 The temperature sensed by the pyrometer for the fixed laser power of 250 W. The temperature sensed by the pyrometer for the fixed laser power of 250 W. The sensed temperature was increased during the build

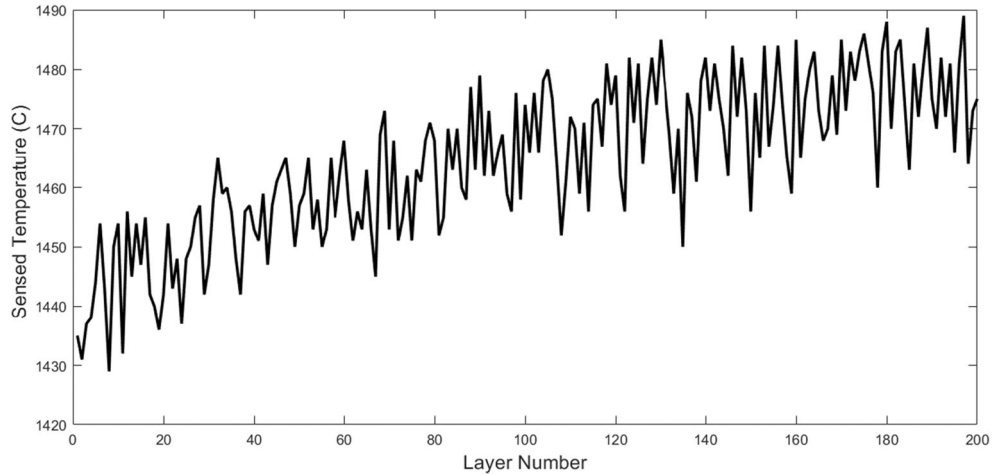


Fig. 22 PDAS variations in different sections while using fixed laser power and controllers for the desired temperature of 1450 °C

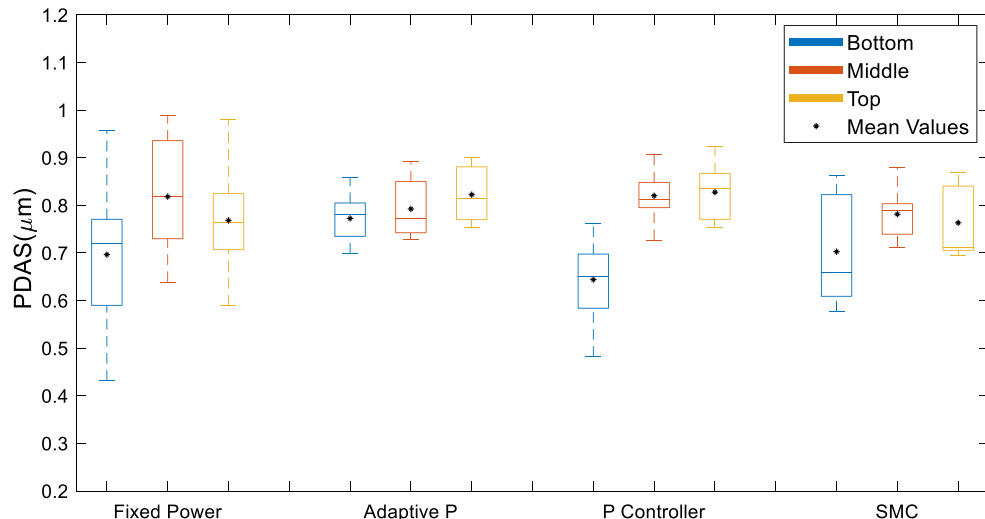
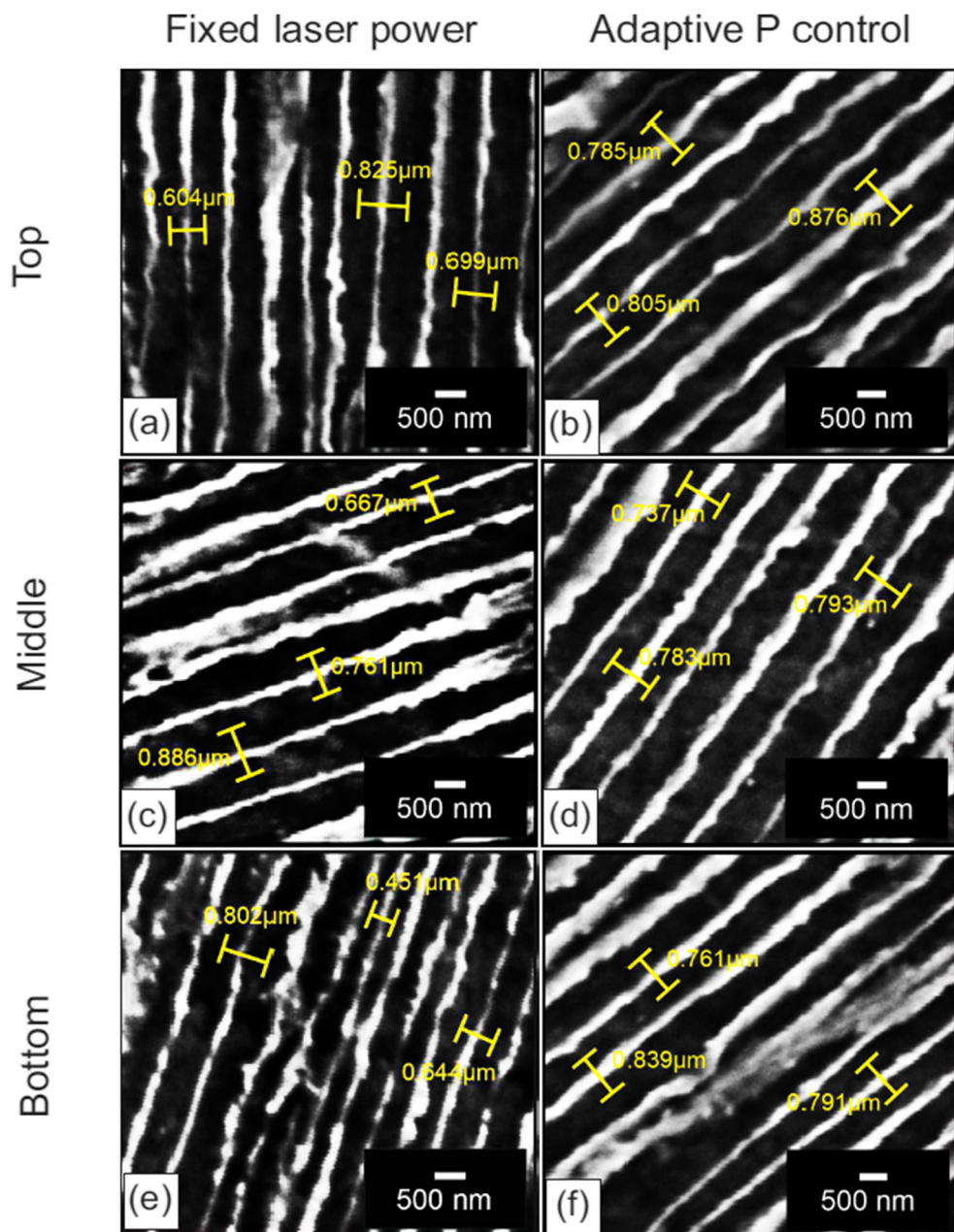


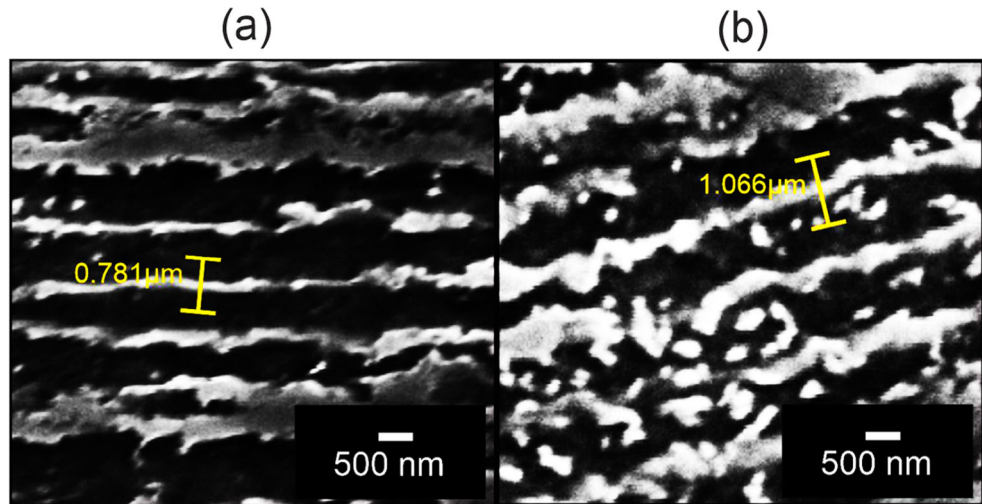
Fig. 23 SEM micrographs of parts with the (a, c, e) fixed set of process parameters and (b, d, f) adaptive P controller (2nd set). The sample measurements are provided in each micrograph



variation in the temperature during the building for the uncontrolled case. The large variations of the PDAS can be traced back to the change in temperature as opposed to the controlled scenario. For instance, LI of the PDAS throughout the part was calculated to be 0.557 μm and 0.165 μm in uncontrolled and adaptive P controller cases, respectively. The two other controllers also made the LI of the PDAS shorter in comparison to the fixed laser power case. Then, it can be concluded that when controllers come into action, more uniform microstructures are achievable. The second point that can be inferred from Fig. 20 is that the LI in the bottom region, where the controllers still struggle to reach the desired temperature, is

larger than the middle and top regions. Nevertheless, the LI in the bottom region of the part fabricated by the adaptive P controller is shorter than those of the SMC and simple P controller due to the faster response of the adaptive P controller. The middle and top regions of all controlled samples have virtually the same range of the PDAS, meaning that the process has reached a near-uniform state prior to the middle region. Moreover, the mean value of the PDAS in the uncontrolled case with fixed laser power of 250 W was lower compared to the controlled scenarios in the middle and top regions (Fig. 20). According to Fig. 16, the laser powers during the controlled processes were higher than 300 W in those regions.

Fig. 24 SEM micrographs of the middle region of parts fabricated by the adaptive P controller with the desired temperature of (a) 1450 °C (2nd set) and (b) 1490 °C (1st set)



Given the fact that the higher laser power in controlled cases results in larger melt pools and, consequently, lower cooling rates, the lower mean values of the PDAS in the uncontrolled case are justifiable [24].

The PDAS measurements of the 2nd set of experiments are illustrated in Fig. 22. The same discussion parallel to that of the 1st set of experiments is valid for this case, which is confirmed by the SEM micrographs provided in Fig. 23. According to Fig. 23, a more uniform microstructure is achieved when the adaptive P controller is implemented. It is worth noting that the mean values of the PDAS in the 2nd set of experiments are lower than the 1st set. For example, the mean value of PDAS with the adaptive controller is 1.051 μm at the top of the part when the desired temperature is 1490 °C while it is 0.8225 μm in the 2nd set of experiments. This is originated from the faster cooling rates associated with, the smaller melt pools, which were created at lower temperature and laser power in 2nd set. The high magnification micrographs of the parts (in the middle region) fabricated under adaptive P controllers at desired temperatures of 1450 °C and 1490 °C are shown in Fig. 24, confirming the above discussion. In addition, the LI of the SMC controller changed from 0.391 μm in the 1st set to 0.286 μm in the 2nd set since

the desired melt pool temperature was achieved sooner in the latter case.

4.3 Microhardness results

To study the mechanical properties of the printed parts under controlled and uncontrolled conditions, the microhardness was measured in the building direction, starting from the height of 3 mm. The microhardness measurement results are summarized in Table 6. The following outcomes can be outlined from the microhardness results:

1. The microhardness increased by increasing the desired temperature in a statistically significant manner. The same trend has been observed for Inconel 625 elsewhere in which the increase of the laser power led to higher microhardness values [25].
2. When a controller was deployed, the microhardness range became smaller than the case in which a fixed laser power was utilized. This is attributed to the shorter LI of the PDAS and, therefore, more uniform microstructures achieved by employing the controllers (Figs. 20 and 22).

Table 6 The microhardness features of the samples

Feature	Fixed laser power	Adaptive P (1490 °C)	Adaptive P (1450 °C)	Simple P (1490 °C)	Simple P (1450 °C)	SMC (1490 °C)	SMC (1450 °C)
Min microhardness (HV)	276	320	308	314	300	314	298
Max microhardness (HV)	326	344	332	345	330	350	329
Variations (HV)	50	24	24	31	30	36	31
Mean value (HV)	302.4	334	321.8	330.5	318.8	333.2	315

5 Conclusion

In this study, an analytical-experimental model was developed, and three different types of controllers (adaptive P, SMC, and simple P) were designed to control the temperature of the melt pool by manipulating the laser power. The performance of the controllers was examined with the existing model. Also, a monitoring system consists of a two-color pyrometer, which was calibrated previously, was utilized to establish different types of experiments on the L-PBF machine and to investigate the performance of the controllers. To find out the correlation between the control process and uniformity of the final products, the printed samples were investigated from the microstructure and microhardness points of view. The results revealed that the thermal dynamics of the melt pool, specifically the temperature, has a great impact on the microstructural and mechanical properties uniformity of the final products. In summary, the following conclusions are derived:

1. Among the proposed controllers, the adaptive P has the fastest response to any deviations from the reference temperature, making it a suitable choice when a time-variable temperature is preferable.
2. A smaller initial error of the temperature can reduce the rise time of all controllers. Therefore, the knowledge about the initial temperature can be helpful in controlling the melt pool temperature.
3. Higher melt pool temperatures result in larger primary dendrite arm spacing (PDAS) which can be attributed to the melt pool enlargement and the reduced cooling rate.
4. The length of interval (LI) of the PDAS is shorter in the controlled cases in comparison to the case subjected to a fixed set of process parameters, especially in the middle and top regions of the samples. This results in a more uniform microstructure throughout the part. It is worthwhile to mention that when using an adaptive P controller, the bottom region of the part shows a narrow LI of the PDAS, which is close to those of the middle and top regions.
5. Implementation of a controller can narrow down the variations of the microhardness along the building direction, leading to more uniform mechanical properties.

Authors' contributions Hossein Rezaifar: investigation, methodology, conceptualization, writing-original draft. Mohamed Elbestawi: review and editing, supervision.

Compliance with ethical standards

Ethical approval Not applicable.

Consent to participate Not applicable

Consent to publish Authors grant the publisher the sole and exclusive license of the full copyright in the contribution.

Competing interests The authors declare that they have no competing interests.

References

1. Lo YL, Liu BY, Tran HC (2019) Optimized hatch space selection in double-scanning track selective laser melting process. *Int J Adv Manuf Technol* 105:2989–3006. <https://doi.org/10.1007/s00170-019-04456-w>
2. Everton SK, Hirsch M, Stavroulakis PI, Leach RK, Clare AT (2016) Review of in-situ process monitoring and in-situ metrology for metal additive manufacturing. *Mater Des* 95:431–445. <https://doi.org/10.1016/j.matdes.2016.01.099>
3. Foster BK, Reutzel EW, Nassar AR, Dickman CJ, Hall BT (2015) A brief survey of sensing for metal-based powder bed fusion additive manufacturing. In: Dimensional Optical Metrology and Inspection for Practical Applications IV, vol 9489, p 94890B. <https://doi.org/10.1117/12.2180654>
4. Chua ZY, Ahn IH, Moon SK (2017) Process monitoring and inspection systems in metal additive manufacturing: status and applications. *Int J Precis Eng Manuf Green Tech* 4:235–245. <https://doi.org/10.1007/s40684-017-0029-7>
5. Fereiduni E, Ghasemi A, Elbestawi M (2020) Selective laser melting of aluminum and titanium matrix composites: recent progress and potential applications in the aerospace industry. *Aerospace* 7. <https://doi.org/10.3390/AEROSPACE7060077>
6. Zeinali M, Khajepour A (2010) Height control in laser cladding using adaptive sliding mode technique: theory and experiment. *J Manuf Sci E T ASME* 132:1–10. <https://doi.org/10.1115/1.4002023>
7. Mohr G, Altenburg SJ, Hilgenberg K (2020) Effects of inter layer time and build height on resulting properties of 316L stainless steel processed by laser powder bed fusion. *Addit Manuf* 32:101080. <https://doi.org/10.1016/j.addma.2020.101080>
8. Silva BL, Araujo IJC, Silva WS, Goulart PR, Garcia A, Spinelli JE (2011) Correlation between dendrite arm spacing and microhardness during unsteady-state directional solidification of Al-Ni alloys. *Philos Mag Lett* 91:337–343. <https://doi.org/10.1080/09500839.2011.559911>
9. Turhal MŞ, Savaşan T (2003) Relationships between secondary dendrite arm spacing and mechanical properties of Zn-40Al-Cu alloys. *J Mater Sci* 38:2639–2646. <https://doi.org/10.1023/A:1024434602540>
10. Fox J, Lopez F, Lane B, Yeung H, Grantham S. On the requirements for model-based thermal control of melt pool geometry in laser powder bed fusion additive manufacturing. In: Proceedings of the 2016 Material Science & Technology Conference 2016 Oct 23, Salt Lake City, pp 133–140
11. Mercelis P, Kruth JP, Van Vaerenbergh J (2007) Feedback control of selective laser melting. In: Proceedings of the 15th International Symposium on Electromachining. ISEM 2007
12. Craeghs T, Bechmann F, Berumen S, Kruth J-P (2010) Feedback control of Layerwise Laser Melting using optical sensors. *Phys Procedia* 5:505–514
13. Renken V, Albiner S, Goch G, Neef A, Emmelmann C (2017) Development of an adaptive, self-learning control concept for an additive manufacturing process. *CIRP J Manuf Sci Technol* 19:57–61. <https://doi.org/10.1016/j.cirpj.2017.05.002>
14. Renken V, Lübbert L, Blom H, Von Freyberg A, Fischer A (2018) Model assisted closed-loop control strategy for selective laser melting. *Procedia CIRP* 74:659–663. <https://doi.org/10.1016/j.procir.2018.08.053>
15. Renken V, von Freyberg A, Schünemann K, Pastors F, Fischer A (2019) In-process closed-loop control for stabilising the melt pool

- temperature in selective laser melting. *Prog Addit Manuf* 4:411–421. <https://doi.org/10.1007/s40964-019-00083-9>
- 16. Ning J, Sievers D, Garmestani H, Liang S (2019) Analytical modeling of in-process temperature in powder bed additive manufacturing considering laser power absorption, latent heat, scanning strategy, and powder packing. *Materials*. 12. <https://doi.org/10.3390/ma12050808>
 - 17. Carslaw HC, Jaeger JC (1959) Conduction of heat in solids. Oxford University Press, Oxford
 - 18. Hägglund T, Åström KJ (1990) An industrial adaptive PID controller. *IFAC Proc Vol* 23:251–256. [https://doi.org/10.1016/s1474-6670\(17\)52729-9](https://doi.org/10.1016/s1474-6670(17)52729-9)
 - 19. El Rifai K (2009) Nonlinearly parameterized adaptive PID control for parallel and series realizations. In: 2009 American Control Conference, June 2009 St. Louis, pp 5150–5155
 - 20. Augusto JS (2010) Fixed and adaptive PID control of the temperature in a laboratory oven. 9–11
 - 21. Astrom KJ, Wittenmark B (1995) Adaptive control. Addison-Wesley, Boston
 - 22. Park K-B (2000) Discrete-time sliding mode controller for linear time-varying systems with disturbances. *Trans Control Autom Sci Eng* 2:244–247
 - 23. Marchese G, Garmendia Colera X, Calignano F, Lorusso M, Biamino S, Minetola P, Manfredi D (2017) Characterization and comparison of Inconel 625 processed by selective laser melting and laser metal deposition. *Adv Eng Mater* 19. <https://doi.org/10.1002/adem.201600635>
 - 24. Qiu C, Chen H, Liu Q, Yue S, Wang H (2019) On the solidification behaviour and cracking origin of a nickel-based superalloy during selective laser melting. *Mater Charact* 148:330–344. <https://doi.org/10.1016/j.matchar.2018.12.032>
 - 25. Brown CU, Jacob G, Possolo A, Beauchamp C, Peltz M, Stoudt M, Donmez A The effects of laser powder bed fusion process parameters on material hardness and density for nickel alloy 625. *NIST Adv Manuf Ser*:100–119. <https://doi.org/10.6028/NIST.AMS.100-19>

Publisher's note Springer Nature remains neutral with regard to jurisdictional claims in published maps and institutional affiliations.